IVYSPRING INTERNATIONAL PUBLISHER

Theranostics

2020; 10(6): 2509-2521. doi: 10.7150/thno.39403

Research Paper

Deep tissue photoacoustic imaging of nickel(II) dithiolene-containing polymeric nanoparticles in the second near-infrared window

Byullee Park[1*], Kyung Min Lee[2,6*], Suhyeon Park[3], Misun Yun[4], Hak-Jong Choi[4], Jeesu Kim[1], Changho Lee[3,5✉], Hyungwoo Kim[6✉], and Chulhong Kim[1✉]

1. Departments of Creative IT Engineering, Electrical Engineering, and Mechanical Engineering, Pohang University of Science and Technology (POSTECH), 77 Cheongam-ro, Pohang 37673, Republic of Korea.
2. Department of Materials Science and Engineering, College of Engineering, Seoul National University, Seoul 08826, Republic of Korea.
3. Interdisciplinary Program of Molecular Medicine, Chonnam National University, 77 Yongbong-ro, Buk-gu, Gwangju 61186, Republic of Korea.
4. Microbiology and Functionality Research Group, World Institute of Kimchi, 86 Kimchi-ro, Gwangju 61755, Republic of Korea.
5. Department of Nuclear Medicine, Chonnam National University Medical School & Hwasun Hospital, 264, Seoyang-ro, Hwasun-eup, Hwasun-gun, Jeollanam-do 58128, Republic of Korea.
6. School of Polymer Science and Engineering, Chonnam National University, 77 Yongbong-ro, Buk-gu, Gwangju 61186, Republic of Korea.

* These authors contributed equally to this work.

✉ Corresponding authors: Chulhong Kim, E-mail: chulhong@postech.edu; Changho Lee, E-mail: ch31037@jnu.ac.kr; Hyungwoo Kim. E-mail: kimhw@jnu.ac.kr.

Received: 2019.08.16; Accepted: 2019.12.22; Published: 2020.01.22

Abstract

Photoacoustic imaging is gaining great attention in the medical world due to its significant potential for clinical translation. Light excitation in the second near-infrared (NIR-II) window (1000-1350 nm) has resolution and penetration depth suitable for several clinical applications. However, the significant challenge exists for clinical translation because of the absence of notable intrinsic chromophores in this clinically significant optical range to generate diagnostic images.

Methods: We present newly developed a biocompatible nickel dithiolene-based polymeric nanoparticle (NiPNP), which have a strong and sharp absorption peak at 1064 nm, as a photoacoustic contrast agent to boost specific absorbance in the NIR-II window for *in vivo* deep tissue imaging.

Results: We confirm the enhanced PA signal by NiPNP's strong light absorption in the NIR-II window (287% higher than that of NIR-I) and deep tissue imaging capability (~5.1 cm) through *in vitro* experiment. We have successfully acquired diagnostic-quality *in vivo* photoacoustic images in deep tissue (~3.4 cm) of sentinel lymph nodes, gastrointestinal tracts, and bladders of live rats by using clinically viable imaging system.

Conclusions: Our results prove that with strong absorption in the NIR-II window and with deeper imaging depth, the clinical translation of photoacoustic imaging with NiPNP is feasible for preclinical studies and thus would facilitate further clinical investigations.

Key words: Photoacoustic imaging, Deep tissue imaging, Nickel dithiolene complex, Polymeric nanoparticle, Second near-infrared window.

Introduction

Photoacoustic imaging (PAI) is a rapidly growing non-invasive imaging modality that has proven its feasibility in preclinical and clinical investigation [1-7]. The PAI provides structural and functional information of live animals and human tissues based on the optical absorption by intrinsic chromophores such as hemoglobin, melanin, and lipids [8-12]. However, PAI using endogenous

chromophores alone has difficulties in imaging some specific organs such as lymph nodes, gastrointestinal (GI) tracts, and bladders due to their optical transparency. Consequently, it is difficult to achieve high sensitivity and specificity to diagnose diseases related to these specific organs. In addition, optical absorption by unwanted intrinsic chromophore present within the tissue generates background noise, resulting in low image contrast in PAI [13-16]. To overcome these obvious disadvantages of intrinsic molecular PAI, it is essential to design exogenous agents with strong light absorption properties at the appropriate optical wavelength to generate high quality diagnostic PA images.

Various studies using exogenous contrast agents and near-infrared (NIR) light have been conducted to overcome the limitations of intrinsic chromophores in PAI [17-25]. In particular, the low attenuation of NIR light compared to the visible light in the tissue is advantageous for acquiring deep tissue PAI *in vivo* [26, 27]. Many studies were performed with methylene blue, indocyanine green, and various nanoparticles as the exogenous agent in the first NIR window (NIR-I, 650-950 nm) [28-34]. Recently, PAI using the second NIR window (NIR-II, 1000-1650 nm) light has received much attention than with the NIR-I because of the following reasons: (1) low photon energy at the longer wavelengths is more suitable for preclinical and clinical studies since they reduce tissue damages; (2) the NIR-II light gets less scattered in biological tissues and avoids absorption by the intrinsic chromophores to minimize background noise and maximize penetration depth; (3) compared to lasers available in the NIR-I window, the 1064-nm Nd:YAG lasers are inexpensive, widely available, and more compact possibly leading to a commercial PAI system beyond research. In addition, because the 1064-nm Nd:YAG lasers have already been used widely in clinical areas such as dermatology, it is well suited for translational research [35-46]. The main challenges for performing PAI in the NIR-II window and applying to preclinical and clinical fields hinge on the design of PA contrast agents that can effectively absorb the NIR-II light and their feasibility of *in vivo* PAI [47-51]. Several studies have been reported in the literature on NIR-II light absorption agents, e.g., gold nanorods [36, 44], narrow-bandgap polymer nanoparticles [40, 41, 43], phosphorus phthalocyanines [39], copper sulfide nanoparticles [37], silver nanoplates [35, 42], perfluorocarbon nanodroplet [38]. Even though the agents above confirmed the possibility of using a 1064-nm laser as an excitation source for PAI, most *in vivo* studies could be performed only at shallow depths [35, 37, 39-41, 43, 44]. Moreover, some agents showed their absorbance positioned predominantly in NIR-I region rather than NIR-II (inefficient absorption in NIR-II window) [37, 42] and were not even feasible for *in vivo* PAI [36, 38]. Recently, a cyanine-based agent was reported as a form of surfactant-stripped micelle and provided notable deep-tissue imaging in NIR-II window [52]. However, it is a still rare case of using small-molecule dyes so far, and other various NIR-II absorbing organic dyes are worth further investigation [53].

In this study, we are the first to report a nickel dithiolene-based polymeric nanoparticle (NiPNP) as a PAI contrast agent that strongly absorbs the NIR-II light with a peak at 1064 nm for *in vivo* deep tissue PAI. Many dithiolene complexes have been investigated widely for non-linear optics, telecommunication, thermoelectrics, or catalytic hydrogen evolution due to unique optical and electronic properties as well as redox and catalytic activities [54]. In particular, nickel dithiolene complexes have attracted attention because of thermo- and photostability and their distinctive photophysical properties including broad NIR absorbance window, which can be further tailored by altering chemical structure of peripheral ligands [55-59]. However, the limited solubility of the complex reduces processability and restricts other potential applications. We used bis(4-dimethyl-aminodithiobenzil)nickel(II) for deep tissue PAI, and prepared nanosized particles (~130 nm) benefitted from an FDA-approved poly(lactide-*co*-glycolide) (PLGA) via nanoprecipitation [60]. The core complex was reported show a high molar extinction coefficient (ε, 2.8×10^4 M/cm at 1060 nm) in the NIR region [57] and also high photochemical stability when used in nonlinear optics or optoelectronics [56, 61, 62], which are sought-after, essential properties for the NIR bio-imaging. Therefore, we could demonstrate the facile preparation of the strong NIR-II absorbing and biocompatible PAI agent that is comprised of the photoactive core and the PLGA shell. The NiPNP disperses stably in an aqueous medium and exhibits strong NIR absorption between 800–1300 nm with a peak at 1064 nm attributed to the electron transition in the nickel complex and is most suitable for NIR-II PA imaging in deep tissues.

Materials and Methods

Materials

Bis(4-dimethylaminodithiobenzil)nickel(II) was purchased from TCI (Tokyo, Japan) and poly(lactic-*co*-glycolic acid) (PLGA; Resomer® RG 503H) from Aldrich. The PLGA consists of 50:50 lactic acid–glycolic acid with a weighted average molecular weight (M_w) ranging from 24 to 38 kDa. All reagents

used were purchased commercially and were used as is unless otherwise noted.

Optical and physical characterization

Transmission electron microscopy (TEM) image was obtained using by a JEM-3010 (JEOL, JPN) operating at 300 kV. The sample solution was dropped on a carbon-coated copper grid and dried under vacuum at room temperature for 24 h. The analytical work was performed by energy-dispersive X-ray spectroscopy (EDS, Oxford Instruments, UK), equipped in TEM. Hydrodynamic particle size and zeta potential were recorded using an electrophoretic light scattering analyzer (ELS-8000, Otsuka Electronics). Optical absorption spectra were measured using a UV–Vis–NIR spectrophotometer (V-770, JASCO). Fourier-transform infrared spectroscopy (FT-IR) were performed using an Attenuated total reflectance Fourier-transform infrared spectroscopy (ATR-FTIR, IFS66/S, Bruker, USA).

Synthesis of NiPNP

NiPNP was synthesized by a typical nanoprecipitation method with minor modification. Bis(4-dimethylaminodithiobenzil)nickel(II) (80 mg, 0.127 mmol) was added to a solution of poly(lactic-*co*-glycolic acid) (PLGA; 267 mg) in acetone (80 mL). After a brief bath sonication, the resulting solution was introduced dropwise to the deionized (DI) water (200 mL) for 10 min while stirring vigorously. The mixture was further stirred for 24 h in a fume hood at 60 °C to remove the acetone and filtered using a 0.2-μm syringe filter to afford a colloid of NiPNP (17 mg/mL). The concentration of dispersion was adjusted by adding DI water for dilution, or by evaporating under reduced pressure and re-adding desired amounts of DI water for higher concentrations.

In vitro toxicity study

The mouse fibroblast L929 cell was purchased from the Korean cell line bank, and MTT kit and live/dead assay were performed to analyze the L929 cell growth under treatment with NiPNP. The cells were harvested and counted, and seeded into 96-well plates at the density of 5,000 viable cells per well and then incubated overnight. 48 hrs after treatment, MTT kit solution was added to the cells and incubated for 24 hrs at 37 ^{o}C. The amount of formazan produced was measured at 562 nm wavelength using an infinite M200 PRO microplate reader. Under same experimental condition, we conducted live/dead assay after incubating NiPNP treated cells during 30 minutes at 20-25^{o}C and took florescent microscopic images.

In vivo toxicity study

Six white Balb/c mice were prepared for *in vivo* toxicity studies by intravenously injecting NiPNP with a concentration of 17.3 mg/mL of 100 μL. Three mice with PBS intravenous injection were used for the control group. 7 and 28 days after the injection of NiPNP, histological and blood analyses were performed on critical organs (i.e., liver, lung, kidney, spleen, heart). Histological data of these organs were fabricated by following the conventional H&E staining process. The blood biochemistry and complete blood cell count were measured.

ICP-MS experiments of extracted organs

NiPNP and PBS were intravenously injected (100 mg/kg) into 6-week female normal Balb/c mice *(n=5 for NiPNP and n=3 for PBS)*. After 24 hours, a mouse was completely anesthetized via a vaporized-isoflurane kit and sacrificed by cervical dislocation. Then, the liver, kidneys, spleen, heart and lungs were extracted. After weighting these organs, they were fully dissolved via fresh aqua regia (5 mL) and heated at 130 ^{o}C. By diluting this solution with DI water, ICP-MS (NexION 350D, Perkin-Elmer SCIEX) calculated the concentration of Ni.

Photoacoustic imaging system

We used two PAI systems: one for *in vitro* and the other for *in vivo and ex vivo* experiments. First, for *in vitro* imaging, an acoustic-resolution photoacoustic microscopy (AR-PAM) system which was introduced in our previous study [10] was used to analyze the photoacoustic (PA) characteristics of NiPNP (Figure S1). Second, for *in vivo and ex vivo* PA and ultrasound (US) imaging, a clinical PA/US system was used to acquire the data. The clinical PA/US imaging system (Figure S2) was divided into an FDA approved programmable US imaging system (EC-12R, Alpinion Medical Systems) and a portable laser system (Phocus, OPOTEK). The laser consisted of an Nd: YAG pumping source and a tunable OPO, which allowed selective use of wavelengths of 532, 1064 and 680 – 900 nm as a PA excitation source. The laser illumination of the selected wavelength was coupled with the bifurcated fiber bundles connected to the laser body. The US imaging system connected to a transducer (L3-12, Alpinion Medical Systems, 8.5 MHz center frequency with a fractional bandwidth of 95%) transmitted and received US signals to form US image and also received the PA signals generated by the laser to form PA image. The US imaging system was synchronized with the laser system by the trigger signal that the laser system sent every pulse. The US transducer and the bifurcated fiber bundle were inserted into the adapter, fixed with forceps, and

connected to a single axis motor. For the volumetric *in vivo* PA/US imaging, Y direction raster scanning was performed by the single axis motor.

In vitro, *in vivo*, and *ex vivo* PA experiments

The AR-PAM system was used for *in vitro* PA experiments. Eight tubes (508-001, Silastic Laboratory Tubing, Dow Corning, USA), similar in size to the blood vessel, were filled with NiPNP having a concentration of 34.6, 17.3, 11.5, 6.8, 3.4, 1.7, 0.8 and 0 mg/mL. The PA spectra were measured from 680 to 1064 nm. For the NiPNP with a concentration of 17.3 mg/mL, additional PA spectra from 1200 to 1350 were also measured. The laser power for each wavelength was measured using a power meter (S350C, Thorlabs, USA) and the power was adjusted to the same value by adjusting the Q-delay of the laser. For the *in vitro* PAI of NiPNP in deep chicken breast tissues, the laser of the AR-PAM system and the programmable US imaging system were used together. The 1064 nm laser fluence used in the experiment was 40 mJ/cm^2, well below the American National Standards Institute (ANSI) laser safety limit of 100 mJ/cm^2. For the sample preparation, a 1 mL of NiPNP with a concentration of 17.3 mg/mL was injected into the microtube, and the microtube was sealed with a silicone mixture to prevent bubble formation. Five layers of 1-cm-thick chicken breasts tissue were stacked on prepared tubes (Figure S3), and two-dimensional depth-resolved PA images were obtained at each layer. To improve the signal-to-noise ratio (SNR) of the PA image, a total of 100 images were collected at the same spatial location and averaged.

The clinical PA/US imaging system was used for *in vivo* sentinel lymph nodes (SLNs), GI tracts, and bladders PA imaging of rats. Pulsed laser at a 1064 nm (30 mJ/cm^2) was used for *in vivo* experiments. All animal experimental procedures were performed in accordance with laboratory animal use protocol approved by the institutional animal care and use committee of the Pohang University of Science and Technology. Healthy rats (~200 g) were prepared to acquire PA/US images. A vaporized-isoflurane system (1 L/min of oxygen and 0.75% isoflurane) was used to initially anesthetize rats and maintain anesthesia during the experiment. After acquiring control PA images for SLN, GI tract, and bladder, NiPNP was delivered through hypodermic injection, oral administration, and transurethral injection (0.1, 0.3, and 0.2 mL of 17.3 mg/mL, respectively) into three different targets, respectively. After a certain time lapse, PA images were obtained at the same location as the control PA images. In the case of PA SLNs, *ex vivo* PA images were obtained by dissecting NiPNP-containing lymph nodes and normal lymph nodes, to validate the *in vivo* results.

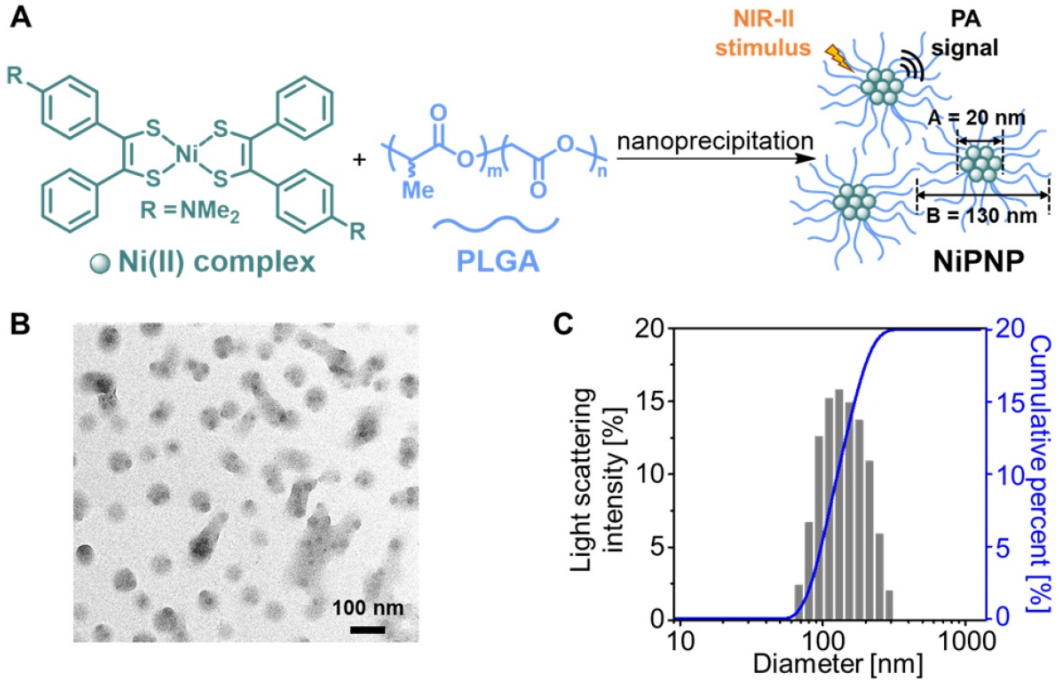

Figure 1. (A) Depiction for the preparation of NiPNP. The core Ni(II) complex (A; diameter, 20 nm) was encapsulated with PLGA via nanoprecipitation to form NiPNP (B; hydrodynamic size, 130 nm). (B) TEM image of NiPNP. (C) Particle size distribution of NiPNP obtained using DLS analysis. NiPNP, Ni(II) complex-containing polymeric nanoparticles; PLGA, poly(lactic-co-glycolic acid); TEM, transmission electron microscope; DLS, dynamic light scattering; NIR, near-infrared.

Results

Synthesis of Ni(II)-containing polymeric nanoparticles and their optical and physical properties

A one-step nanoprecipitation method was used to synthesize the core-shell type NiPNP. The NiPNP contains bis(4-dimethylaminodithiobenzil)nickel(II) (BDN) as a PA-active core material and PLGA as a biocompatible polymer shell, as shown in Figure 1A. The core Ni(II) complex exhibits broad light absorption in the NIR-II window and allows the use of laser pulse at 1064 nm while PLGA encapsulates the core complexes, which significantly increases the penetration depth for deep tissue imaging. Therefore, after precipitation process, the nanoparticle agent was obtained which showed the desired absorption spectrum in the NIR-II window in water. Figure 1B shows the core–shell structure of NiPNPs in which the size of the photoactive BDN core in NiPNPs measured an average of 20 ± 2.6 nm when observed by TEM. The EDS equipped in TEM confirmed the chemical composition of an individual NiPNP particle including elemental Ni(II) (Figure S4). We also investigated a hydrodynamic diameter of the nanoparticles including the polymer shell through dynamic light scattering measurement which reflects a fully extended, overall size of particle under aqueous conditions, and found the value of 130 ± 52 nm with a uniform distribution (polydispersity index of 0.10) (Figure 1C). FT-IR investigation further revealed the inclusion of the metal complex and PLGA to afford NiPNP (Figure S5).

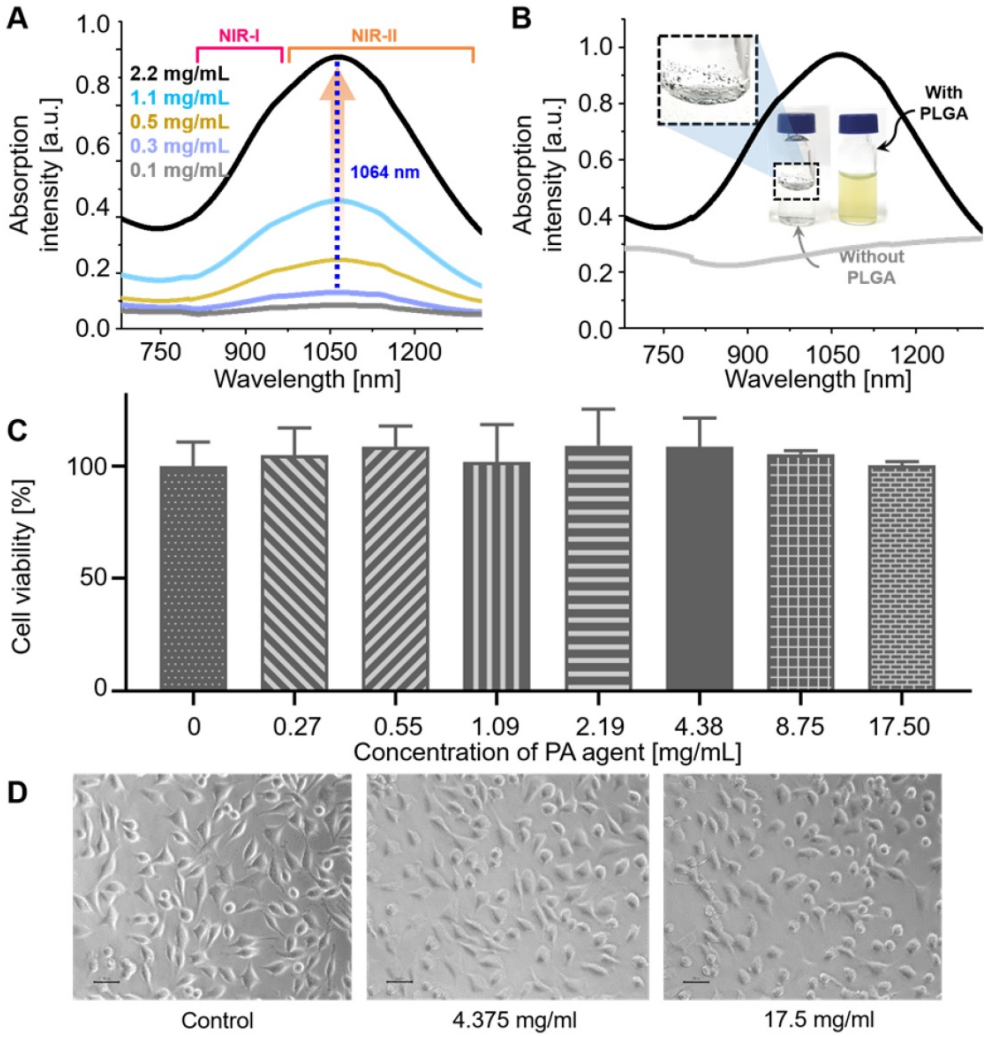

Figure 2. (A) NIR-I and -II absorption spectra of NiPNP measured at different concentrations from 0.1 to 2.2 mg/mL. The maximum absorption peak appears at 1064 nm (dotted blue). (B) NIR-I and -II absorption spectra of NiPNP (with PLGA, black) and the core Ni(II) complex (without PLGA, gray) in water. Without PLGA, the complexes were aggregated and precipitated in water and did not show the absorption spectrum when compared with NiPNP. Photographs of the metal complex (without PLGA, left) and the resulting NiPNP (with PLGA, right) in water. Cell viability of L929 mouse fibroblasts cells treated with NiPNP and phase contrast microscopic images. (C) Cells were treated with NiPNP at indicated concentration for 48 h and the amount of viable cells were measured by MTT kit. (D) Microscopic images after NiPNP incubated with cells (40 ×). Data are presented as the mean ± SD of three independent experiments. (Scale bar 30 μm) NiPNP, Ni(II) complex-containing polymeric nanoparticles; PLGA, poly(lactic-co-glycolic acid); TEM, transmission electron microscope;; NIR, near-infrared.

As designed, NiPNP showed NIR absorbance in the NIR-II region (Figure 2A) with the maximum absorption intensity at 1064 nm. The optical absorption of NIR-II at 1064 nm was about 257% higher than that of NIR-I at 700 nm. The absorption intensity at 1064 nm proportionally increased with the increase in the concentration of NiPNP from 0.1 to 2.2 mg/mL and the photographs of NiPNP revealed a yellowish green color that grew richer in proportion to the concentration (Figure S6). The contrast agent was considerably stable in water because of the PLGA shell that rendered dispersibility and biocompatibility in aqueous media. For example, we were still able to find the same absorption spectrum (Figure S7A) and particle size distribution (Figure S7B) after storing the contrast agent for 3 months at room temperature. The photograph taken after the storage was similar as before without severe aggregation (Figure S7C). Without PLGA, absorption in the NIR-II region was not completely developed (Figure 2B), and only aggregation of the complexes was observed (inset in Figure 2B). Only floating aggregates of the complex were observed on the surface of water (inset in Figure 2B) and the proper investigation of absorbance was thwarted, corroborating the crucial role of PLGA. The zeta potential of the contrast agent was found to be –30.22 mV, further supporting the colloidal stability of NiPNP in water (Figure S8).

In vitro and *in vivo* toxicity

The cytotoxicity of the NiPNP was tested with L929 cell line *in vitro*. The NiPNP demonstrated low toxicity with over 90% cell viability from 0 to 17.5 mg/mL (Figure 2C). Furthermore, no significant cell damages were observed on microscopic images (Figure 2D) and live/dead florescent microscopic images (Figure S9). *In vivo* toxicity testing of NiPNP was also conducted. After intravenous injection of NiPNP, the white Balb/c mice behavior was observed for 1 month, but no symptoms of toxicity were observed. Three mice were sacrificed at 7 and 28 days, respectively, and the mice injected with PBS were prepared as the control group. After extracting the major organs (hearts, lungs, livers, kidneys, and spleens) of the mouse, the histological data were prepared according to the general hematoxylin and eosin (H & E) staining method (Figure S10). No specific organ damage or inflammation was found at 7 and 28 days, showing similar results as the control. In order to investigate the possibility of further toxicity, a complete blood count test and blood biochemistry were tested at 7 and 28 days after injecting NiPNP (100 mg / Kg) into white Balb/c mice. The measured values were shown in the normal range (Figure S11). Thus, toxicity test results indicate that the biocompatibility of NiPNP was high for at least 28 days and within the dose used. ICP-MS analysis method was also conducted to estimate remaining the NiPNP in the main internal organs 24 hrs after intravenous injecting the NiPNP (Figure S12). The remained Ni concentration in organs (kidney, lung, liver, spleen, and heart) were not significant compared with PBS injection data (NiPNP, 0.49 ± 0.02, 8.10 ± 5.13, 3.60 ± 3.11, 1.77 ± 1.03, and 0.53 ± 0.33 ng Ni per mg tissue; PBS 0.16 ± 0.13, 0.20 ± 0.30, 0.07 ± 0.05, 0.58 ± 0.72, and 0.42 ± 0.36 µg Ni per mg tissue).

In vitro PA experiments and properties

The measured optical absorption intensity of NiPNP follows a Gaussian distribution with a peak at 1064 nm in the NIR-II region (Figure 2A). To observe the PA characteristics of NiPNP, we prepared 8 vessel mimicking tubes with different concentrations of the NiPNP and measured the PA signals using an AR-PAM system [10]. As the NiPNP concentration increased, the PA amplitude also increased, and the strongest PA signals were generated by the 1064 nm wavelength in all different concentrations (Figure S13). For bioimaging in an animal model, the NiPNP concentration of 17.3 mg/mL was selected due to its high optical absorption and low toxicity with over 90% cell viability. The PA spectrum of the NiPNP with a concentration of 17.3 mg/mL was measured from 700 nm to 1350 nm, and confirmed that the PA spectrum (Figure 3A) is almost identical to the optical spectrum. The PA amplitude of NIR-II at 1064 nm was about 287% higher than that of NIR-I at 700 nm. In addition, the PA sensitivity of NiPNP at 1064 nm was measured at different concentrations (Figure 3B). PA signals have a linear relationship with concentration by default, but because they contain nonlinear components (e.g., response of the transducer and plastic tubes), it is difficult to represent a complete linear relationship in the experiment. However, looking at the minimum to maximum concentrations, overall linearity trend was identified. PA spectrum and PA sensitivity graphs were normalized to 1 at 1064 nm and 17.3 mg/mL, respectively. In addition, the PA response was obtained for 10 mJ/cm^2 pulse energy at 1064 nm to verify the photostability of NiPNP with a concentration of 17.3 mg/mL (Figure S14). The light energy was appropriately selected based on the penetration depth of 1/e, assuming agents are placed in the tissue. The PA amplitude of the NiPNP shows a fairly stable result even while 3000 laser pulses (5 mins) were irradiated to the sample (Figure S14A). Also, NiPNP before laser irradiation and NiPNP after laser irradiation of 3000 shots were confirmed by TEM, showing little change in particle shape (Figure S14B). After 3000 shots, the

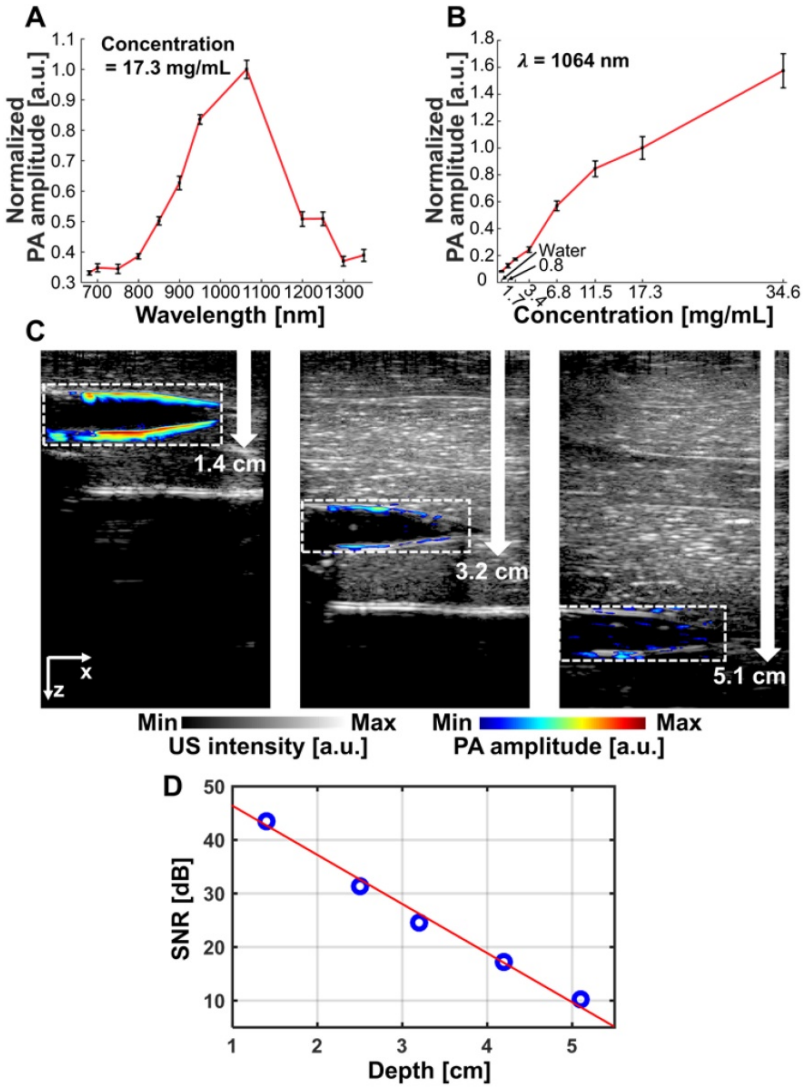

Figure 3. PA characteristics of the NiPNP *in vitro*. (A) PA spectrum of the NiPNP at 17.3 mg/mL concentration. (B) PA sensitivity of the NiPNP at various concentrations with a wavelength of 1064 nm. (C) PA/US overlaid images of the tube filled with NiPNP at different depths prepared with chicken breast tissues. (D) Quantification of PA SNR at different depths. PA, photoacoustic; US, ultrasound; NiPNP, Ni(II) complex-containing polymeric nanoparticles; SNR, signal-to-noise ratio.

PA signal was reduced. To explore the feasibility of using NiPNP as a deep tissue PAI contrast agent, the overlaid PA/US images with NiPNP were acquired at various depths in chicken breast tissues (Figures 3C, D). In the overlaid PA/US images, the PA signal in pseudo color represents the absorption of light in the tube filled with the NiPNP, and the US signal in a gray scale represents the morphological structure of the tube and surrounding chicken tissues (Figure 3C). The reason why the PA signal is observed only at the boundary of the tube is related to the limited bandwidth of the transducer [63]. PA signals generated inside the tube are mainly low frequency components, and PA signals generated at the boundary are mainly high frequency components. However, because the bandwidth of the transducer used in the experiments was relatively high, most low-frequency signals generated inside the tubes could not be detected, which is a typical phenomenon of the bandwidth limited PA detection. The maximum detectable penetration depth for the PA signal was ~5.1 cm with the SNR of 10.2 dB. As the imaging depth increases, the SNR of the PA signal decreases exponentially, and the measured 1/e decay was 0.95 cm (Figure 3D). The experimentally measured PAI depth is 5.3 times greater than the optical penetration depth.

In vivo and *ex vivo* PA experiments

We conducted *in vivo* experiments on rats to confirm that NiPNP with strong absorbance at 1064 nm could be used as the PA agents in deep tissues (Figures 4–6). We imaged clinically important SLN (n = 3), GI tract (n = 3) and cystography (n = 3) [42]. We adopted the rat model because the skin of a rat is more structurally similar to human tissue than other rodents. Figure 4 shows the PA/US images of SLNs, Figure 5 shows those of GI tracts, and Figure 6 shows those of bladders. Panels A–C in Figure 4–6 represents the PA maximum amplitude projection (MAP) images acquired pre-NiPNP injection, post-NiPNP injection without chicken tissues, and post-NiPNP injection with chicken tissues, respectively. Panels D–F of Figure 4–6 are obtained by applying a depth encoded image processing method to the panels A–C, respectively. Panels G–I in Figure 4–6 represent the 2D depth-resolved PA/US images obtained along the white dashed lines in the panels A–C, respectively. Panel J in Figure 4–6 shows the quantification results of PA amplitude enhancement at the NiPNP injection sites (pre-injection, post-injection without chicken tissues, and post-injection with chicken tissues). The imaging region is indicated by the black dashed boxes in the animal photographs as shown in Figure 4K–6K. The PA amplitude enhancement was calculated as the percentage increase in the PA amplitudes pre- and post-NiPNP injection (i.e., $(PA_{after} - PA_{before})/ PA_{before} \times 100$) at the SLNs, GI tracts, and bladders. The error bar denotes the standard error for n = 3.

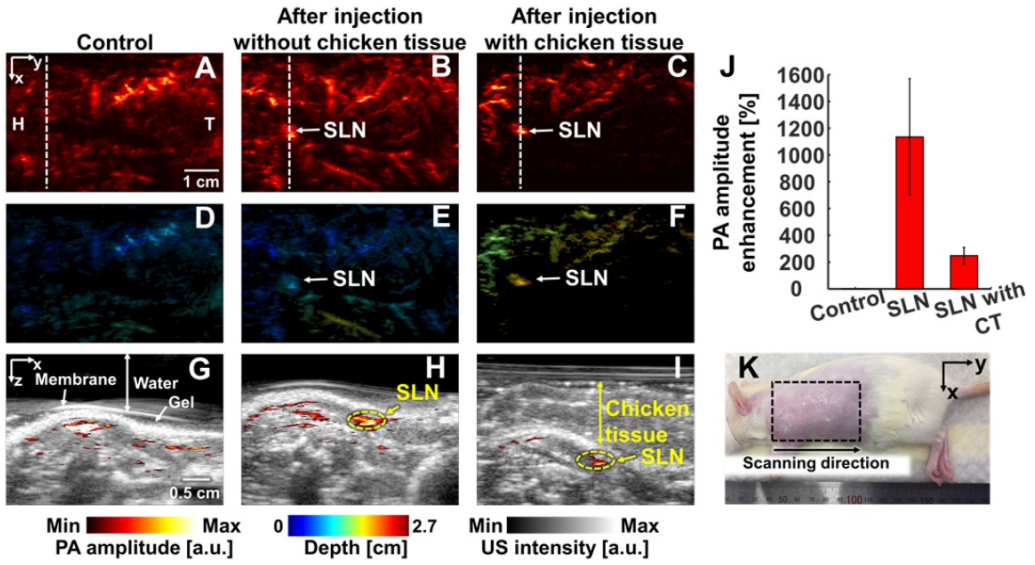

Figure 4. *In vivo* PA imaging of rats SLN (n = 3) using a 1064 nm laser excitation. (A) Before, (B) after without chicken tissue and (C) after with chicken tissue injection of NiPNP PA MAP images. (D-F) obtained by applying depth encoding processing to panel (A-C), respectively. (G-I) Two-dimensional PA/US overlaid images obtained along the white dashed lines in panel (A-C), respectively. (J) PA enhancement comparison before injection of NiPNP, after injection of NiPNP without chicken tissue and after injection of NiPNP with stacking the chicken tissue. (K) Photograph of the rat before *in vivo* PA imaging of SLN. Error bar denotes the standard error of three experiments. PA, photoacoustic; US, ultrasound; NiPNP, Ni(II) complex-containing polymeric nanoparticles; MAP, maximum amplitude projection; SLN, sentinel lymph node; H, head; T, tail; CT, chicken tissue.

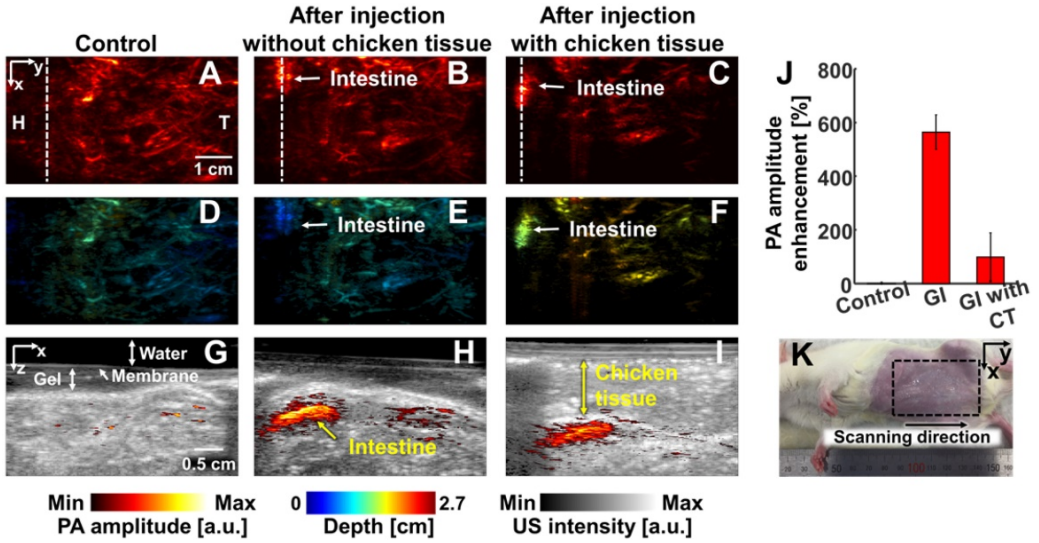

Figure 5. *In vivo* PA imaging of rats GI tract (n = 3) using a 1064 nm laser excitation. (A) Before, (B) after without chicken tissue and (C) after with chicken tissue injection of NiPNP PA MAP images. (D-F) obtained by applying depth encoding processing to panel (A-C), respectively. (G-I) Two-dimensional PA/US overlaid images obtained along the white dashed lines in panel (A-C), respectively. (J) PA enhancement comparison before injection of NiPNP, after injection of NiPNP without chicken tissue and after injection of NiPNP with stacking the chicken tissue. (K) Photograph of the rat before *in vivo* PA imaging of GI tract. Error bar denotes the standard error of three experiments. PA, photoacoustic; US, ultrasound; NiPNP, Ni(II) complex-containing polymeric nanoparticles; MAP, maximum amplitude projection; GI, gastrointestinal; H, head; T, tail; CT, chicken tissue.

PAI of sentinel lymph nodes: We photoacoustically imaged SLNs in the rat model before injecting the NiPNP. It was not visible in the PA image due to the optical transparency in the control image. At 24-hrs-post-injection, the SLN was clearly visualized in the PA image and showed a PA amplitude enhancement of 1135 ± 434% compared to control SLN region. In addition, even after a 1.2-cm-thick chicken breast tissue was placed on the rat, the SLN was visible in the PA images with a PA amplitude enhancement of 248 ± 62%. The depth-encoded PA images and the overlaid PA/US B-mode demonstrated the clear visibility of SLN even at a depth of ~1.5 cm with the chicken breast tissues. To verify the *in vivo* PA SLN imaging results, the draining lymph nodes and control lymph nodes were excised from the axillary region of rats and were imaged using the clinical PA/US imaging system. In *ex vivo* PAI, the only draining SLN is photoacoustically visualized with great PA amplitude enhancement (2697 ± 827%, Figure S15). To confirm the efficiency of NIR-II PAI of NiPNP *in vivo*, NIR-I PAI results were examined (Figure S16). After injection of NiPNP, a weak SLN signal was observed

in PA image obtained by irradiation with 800 nm laser source. Compared with the control PA image, PA amplitude enhancement was 115% and 18% before and after stacking chicken tissues. We confirm that the SNR in the NIR-II is about 6.7 dB higher than that in the NIR-I *in vivo*. Despite the signal observed in the SLN, the NIR-I laser is absorbed more by blood vessels and other tissues than the NIR-II laser, making it difficult to see the clear contrast of the SLN compared to the surroundings.

PAI of GI tracts: We noninvasively and photoacoustically imaged the GI tracts of the small animals with oral administration of NiPNPs. The PA images of the GI tract were acquired before and after 2 hrs post-NiPNP oral administration. Because the rat was starved for 2 days before acquiring the PA image, the PA signals were scarcely visible in the GI tract of the control PA image. In contrast, the GI tract was clearly visible in the PA images obtained post-NiPNP injection with the enhanced PA amplitude (564 ± 63% and 99 ± 90%, respectively) and with/without stacking of the chicken tissues on the abdomen of the rat. In the depth-encoded images and the PA/US overlaid B-mode images, we confirmed that the PA signals enhanced by the NiPNP were visible at a depth of 1.5 cm, including the chicken tissues.

PAI of bladders: In the third application, we imaged the bladders of the small animals with a transurethral injection of NiPNPs noninvasively and photoacoustically. In the PA image acquired before injecting the NiPNP, the bladder is invisible due to transparency at 1064 nm. However, the bladder is clearly visible in the PA images acquired post-NiPNP injection. The calculated PA amplitude enhancements without and with the chicken tissues placed on the rat's abdomen are 918 ± 68% and 238 ± 104%, respectively. The overlaid PA/US B-mode and depth-encoded PA images enhanced by the NiPNP injected into the bladder show that the PA signals are generated at depths of about 1.7 cm, including the chicken breast tissues. Additionally, bladder PA image of a rat was acquired with higher laser power (~ 66 mJ/cm^2) to demonstrate the potential of NiPNP as a PA contrast agent in deeper tissues (Figure S17). As a result, a PA image was obtained from the bladder at a depth of 3.4 cm including chicken tissues, confirming that it was about 200% PA amplitude enhancement compared to the control.

Discussion

The key of deep tissue PAI is to develop agents that are safe and have strong and specific optical absorption properties in the NIR-II. The newly developed contrast agent, namely NiPNP, meets all the above two criteria and we confirmed the feasibility of the NiPNP as a PA contrast agent *in vitro,*

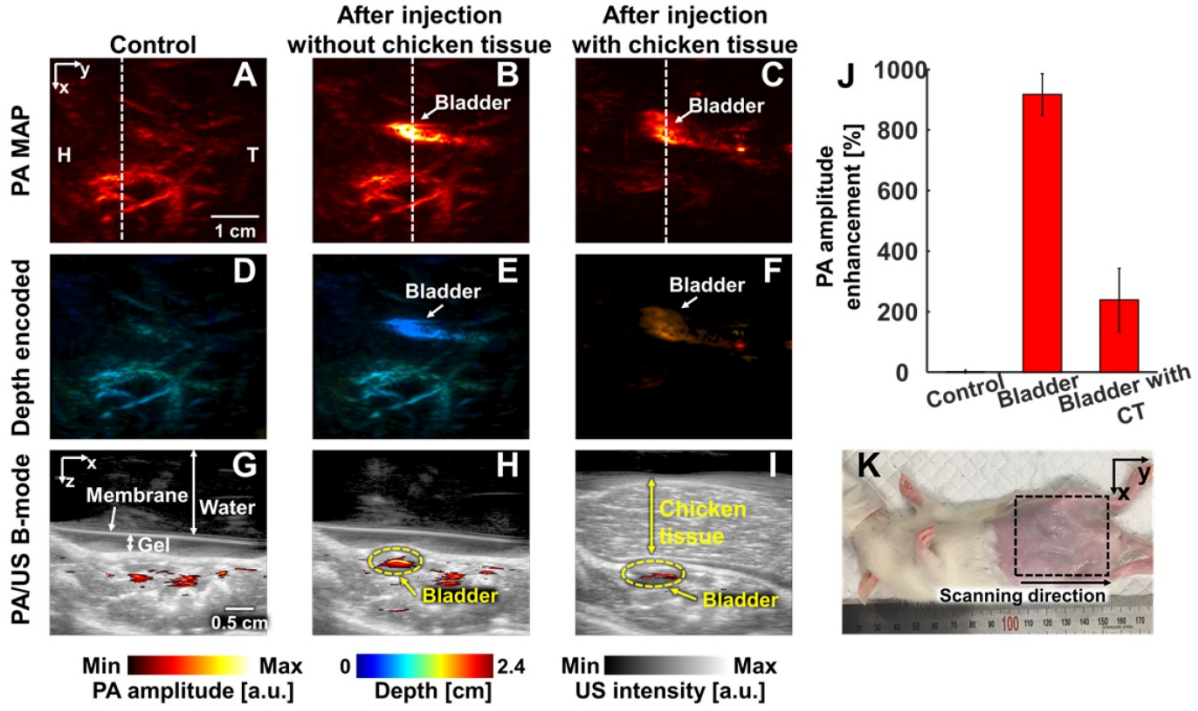

Figure 6. *In vivo* PA imaging of rats bladder (n = 3) using a 1064 nm laser excitation. (A) Before, (B) after without chicken tissue and (C) after with chicken tissue injection of NiPNP PA MAP images. (D-F) obtained by applying depth encoding processing to panel (A-C), respectively. (G-I) Two-dimensional PA/US overlaid images obtained along the white dashed lines in panel (A-C), respectively. (J) PA enhancement comparison before injection of NiPNP, after injection of NiPNP without chicken tissue and after injection of NiPNP with stacking the chicken tissue. (K) Photograph of the rat before *in vivo* PA imaging of bladder. Error bar denotes the standard error of three experiments. PA, photoacoustic; US, ultrasound; NiPNP, Ni(II) complex-containing polymeric nanoparticles; MAP, maximum amplitude projection; H, head; T, tail; CT, chicken tissue.

in vivo, and ex vivo. The polymeric particles were facilely prepared via nanoprecipitation using the nickel(II) bis(dithiolene) complex and PLGA. In brief, when precipitated under aqueous conditions in the presence of PLGA, the BDN particles were encapsulated by the surfactant polymer through physical interaction such as hydrophobic force and stabilized without further coagulation, leading to the formation of core–shell type NiPNPs. As designed, the core-shell particle not only showed biocompatibility and structural stability but also had strong optical absorption in the NIR-II window. The optical absorption at 1064 nm was about 257% higher than that at 700 nm**.** In particular, cell viability with over 90% at 17.5 mg/mL and *in vivo* cytotoxic test including histological data and blood analysis show low toxicity of NiPNP and applicability to future clinical applications. Based on these results, the dose of *in vivo* PA experiment was determined to be 17.3 mg/mL and offered two advantages: excellent biocompatibility and PA contrast.

The PA amplitude characteristics of NiPNP followed the Gaussian distribution in the NIR-II window with a peak at 1064 nm. The PA amplitude at 1064 nm was about 287% higher than that at 700 nm. The maximum depth of the detectable PA signal at 1064 nm in biological tissues was about 5.1 cm. Unfortunately, the laser power used in the *in vitro* PA experiment was limited to 40 mJ/cm^2, corresponding to 40% of the ANSI limit, due to the limitation of the experimental environment. We expected that increasing the laser power to the ANSI safety limit will increase the imaging depth. Although the laser power was not sufficient, our results shows that the NiPNP can serve as a PA contrast agent for clinical application requiring large image depths.

The potential of using NiPNP for preclinical and clinical investigation was demonstrated via *in vivo* and *ex vivo* PAI of SLNs, GI tracts, and bladders in rats, thus could be translated for human clinical evaluation [64-70]. Note that the NiPNP concentration for *in vivo* experiments was performed at 17.3 mg/mL based on cell viability results. To further enhance the possibility of clinical translation, we used the clinical PA/US imaging system with a 1064-nm laser [71, 72]. The three applications each require PAI with extrinsic agents for the following clinical significance: (1) The SLN biopsy, a prognostic indicator of cancer metastasis, using radioactive colloids and colored dyes is a representative method for the staging of metastatic cancer [16]. Ionizing radiation from SLN biopsies is known to have no side effects to patients and physicians if properly followed the regulations, but may be adversely affected by radiation exposure when the does amount, the exposure time, the distance from the radiation source and the shielding are misused [73] . As an alternative to avoid this potential risk, the PAI using extrinsic agents has proven to be a suitable tool for SLN visualization [4, 42, 68]. (2) The GI imaging plays an important role in the diagnosis and treatment of GI related diseases. In particular, intestinal motility disorders cause variety of bowel disorders such as bacterial growth, irritable bowel syndrome, and in many diseases even severe side effects, such as thyroid disorders and diabetes [13, 74]. The X-ray and computed tomography are the leading imaging tools for GI observation. However, these imaging devices use ionizing radiation. Safe, non-invasive and non-ionized PA imaging can be a great alternative imaging tools for GI observation. (3) Bladder imaging is essential for monitoring diseases such as vesicoureteral reflux, cystitis, glomerulation, and bladder cancer. In particular, cystography is the gold standard imaging method for diagnosing bladder related diseases using radio-opaque contrast agents. However, this technique does not have high sensitivity and can negatively affect the prognosis of a patient due to the ionizing radiation used [75]. Comparing the PA images obtained before and after NiPNP injection in *in vivo* applications, we confirmed that the PA signals obtained at the SLNs, GI tracts, and bladders were improved by up to 1135 ± 434%, 564 ± 63% and 918 ± 68%, respectively. In addition, *in vivo* PA images of the rats obtained by increasing the tissue depth using chicken breasts in SLNs, GI tracts and bladders showed 248 ± 62%, 99 ± 90% and 238 ± 104% enhanced PA signal, respectively.

Studies to enhance the PA signals using NIR-II absorbers have recently been published in other studies. However, as mentioned in Introduction section, in most studies, the feasibility of deep tissue PAI was not confirmed, or the light absorption properties of the agents slightly deviated from 1064 nm, which limits the efficiency of the laser. Table S1 shows brief comparison of the major NIR-II PA agents. This study is not only limited to the development of agents with the highest optical absorption properties at 1064 nm, but also it is significant that we have experimentally validated deep tissue PAI using rats with a similar tissue structure to human. Additionally, although NiPNP was verified to be nontoxic, ICP-MS results 24 hours after NiPNP injection confirmed that NiPNP accumulated in major organs. However, ICP-MS results also confirmed that NiPNP could be released as nickel was detected in the kidney. Further research on long-term release due to biodegradation of the particles will be made in subsequent studies.

Conclusion

In this study, we proposed a nickel-based PA agent with sharp peak optical absorption at 1064 nm and verified its potential as a PA contrast agent through various experiments. We have also demonstrated the potential of NiPNP to be used in future clinical applications as a PA contrast agent by successfully obtaining *in vivo* deep tissue PAI using the clinically viable imaging system. These results suggest that the NiPNP would play an effective role as a PA contrast agent, which are required for the diagnosis of various diseases related to deep biological organs.

Abbreviations

PAI: photoacoustic imaging; PA: photoacoustic; US: ultrasound; SNR: signal-to-noise ratio; GI: gastrointestinal; NIR: near-infrared; NiPNP: nickel dithiolene-based polymeric nanoparticle; PLGA: poly(lactide-*co*-glycolide); FT-IR: Fourier-transform infrared; DI: deionized; TEM: transmission electron microscopy; AR-PAM: acoustic-resolution photoacoustic macroscopy; ANSI: american national standard insititute; SLN: sentinel lymph node; MAP: maximum amplitude projection.

Supplementary Material

Supplementary figures and table.
http://www.thno.org/v10p2509s1.pdf

Acknowledgements

The authors thank ICT Consilience Creative program (IITP-2018-2011-1-00783) of the MSIT (Ministry of Science and ICT) supervised by the IITP (Institute for Information & communications Technology Promotion), the Korea Health Technology R&D Project (HI18C0858) through the KHIDI (Korea Health Industry Development Institute) funded by the Ministry of Health & Welfare and the National Research Foundation (NRF) funded by the MSIT (NRF-2019R1A2C2006269 and 2019R1F1A1055458), and the Pioneer Research Center Program through the NRF funded by the MSIT (NRF-2017M3C1A3037762 and 2015M3C1A3056407).

Author Contributions

All authors contributed extensively to this work. C. K., H. K., C. L., B. P., and K. M. L. conceived and designed the study. B. P. and J. K. constructed the hardware system. B. P., S. P., and K. M. L. performed the experiments. B. P., K. M. L., S. P., M. Y., and H. C. analyzed the data. B. P. and K. M. L. wrote the manuscript under the guidance of C. K. and C. K. supervised the study.

Competing Interests

C. Kim has financial interests in OPTICHO, which, however, did not support this work.

References

1. Zhang HF, Maslov K, Stoica G, Wang LV. Functional photoacoustic microscopy for high-resolution and noninvasive *in vivo* imaging. Nat Biotechnol. 2006; 24: 848-51.
2. Kim C, Favazza C, Wang LV. *In vivo* photoacoustic tomography of chemicals: high-resolution functional and molecular optical imaging at new depths. Chem Rev. 2010; 110: 2756-82.
3. Wang LV, Hu S. Photoacoustic tomography: *in vivo* imaging from organelles to organs. Science. 2012; 335: 1458-62.
4. Lee M-Y, Lee C, Jung HS, Jeon M, Kim KS, Yun SH, et al. Biodegradable photonic melanoidin for theranostic applications. ACS Nano. 2015; 10: 822-31.
5. Kim JY, Lee C, Park K, Han S, Kim C. High-speed and high-SNR photoacoustic microscopy based on a galvanometer mirror in non-conducting liquid. Sci Rep. 2016; 6: 34803.
6. Weber J, Beard PC, Bohndiek SE. Contrast agents for molecular photoacoustic imaging. Nat Methods. 2016; 13: 639-50.
7. Li L, Zhu L, Ma C, Lin L, Yao J, Wang L, et al. Single-impulse panoramic photoacoustic computed tomography of small-animal whole-body dynamics at high spatiotemporal resolution. Nat Biomed Eng. 2017; 1: 0071.
8. Yao J, Wang L, Yang J-M, Maslov KI, Wong TT, Li L, et al. High-speed label-free functional photoacoustic microscopy of mouse brain in action. Nat Methods. 2015; 12: 407-10.
9. Razansky D, Distel M, Vinegoni C, Ma R, Perrimon N, Köster RW, et al. Multispectral opto-acoustic tomography of deep-seated fluorescent proteins *in vivo*. Nat Photonics. 2009; 3: 412-7.
10. Lee D, Beack S, Yoo J, Kim SK, Lee C, Kwon W, et al. *In vivo* photoacoustic imaging of livers using biodegradable hyaluronic acid-conjugated silica nanoparticles. Adv Funct Mater. 2018; 28: 1800941.
11. Toi M, Asao Y, Matsumoto Y, Sekiguchi H, Yoshikawa A, Takada M, et al. Visualization of tumor-related blood vessels in human breast by photoacoustic imaging system with a hemispherical detector array. Sci Rep. 2017; 7: 41970.
12. Kim J, Kim Y, Park B, Seo HM, Bang C, Park G, et al. Multispectral *ex vivo* photoacoustic imaging of cutaneous melanoma for better selection of the excision margin. Br J Dermatol. 2018; 179: 780-2.
13. Zhang Y, Jeon M, Rich LJ, Hong H, Geng J, Zhang Y, et al. Non-invasive multimodal functional imaging of the intestine with frozen micellar naphthalocyanines. Nat Nanotechnol. 2014; 9: 631-8.
14. Zackrisson S, Van De Ven S, Gambhir S. Light in and sound out: emerging translational strategies for photoacoustic imaging. Cancer Res. 2014; 74: 979-1004.
15. Srivatsan A, Jenkins SV, Jeon M, Wu Z, Kim C, Chen J, et al. Gold nanocage-photosensitizer conjugates for dual-modal image-guided enhanced photodynamic therapy. Theranostics. 2014; 4: 163-74.
16. Lee C, Kim J, Zhang Y, Jeon M, Liu C, Song L, et al. Dual-color photoacoustic lymph node imaging using nanoformulated naphthalocyanines. Biomaterials. 2015; 73: 142-8.
17. Liu X, Lee C, Law W-C, Zhu D, Liu M, Jeon M, et al. Au–Cu2–x Se heterodimer nanoparticles with broad localized surface plasmon resonance as contrast agents for deep tissue imaging. Nano Lett. 2013; 13: 4333-9.
18. De La Zerda A, Zavaleta C, Keren S, Vaithilingam S, Bodapati S, Liu Z, et al. Carbon nanotubes as photoacoustic molecular imaging agents in living mice. Nat Nanotechnol. 2008; 3: 557-62.
19. Wu Y, Sun L, Zeng F, Wu S. A conjugated-polymer-based ratiometric nanoprobe for evaluating in-vivo hepatotoxicity induced by herbal medicine via MSOT imaging. Photoacoustics. 2019; 13: 6-17.
20. Yang Z, Song J, Tang W, Fan W, Dai Y, Shen Z, et al. Stimuli-responsive nanotheranostics for real-time monitoring drug release by photoacoustic imaging. Theranostics. 2019; 9: 526-36.
21. Yang Z, Chen X. Semiconducting perylene diimide nanostructure: multifunctional phototheranostic nanoplatform. Acc Chem Res. 2019; 52: 1245-54.
22. Yang Z, Song J, Dai Y, Chen J, Wang F, Lin L, et al. Self-assembly of semiconducting-plasmonic gold nanoparticles with enhanced optical property for photoacoustic imaging and photothermal therapy. Theranostics. 2017; 7: 2177-85.
23. Duffy MJ, Planas O, Faust A, Vogl T, Hermann S, Schäfers M, et al. Towards optimized naphthalocyanines as sonochromes for photoacoustic imaging *in vivo*. Photoacoustics. 2018; 9: 49-61.

24. Chen Q, Yu J, Kim K. Optically-triggered phase-transition droplets for photoacoustic imaging. Biomed Eng Lett. 2018; 8: 223-9.
25. Chitgupi U, Lovell JF. Naphthalocyanines as contrast agents for photoacoustic and multimodal imaging. Biomed Eng Lett. 2018; 8: 215-21.
26. Bashkatov A, Genina E, Kochubey V, Tuchin V. Optical properties of human skin, subcutaneous and mucous tissues in the wavelength range from 400 to 2000 nm. J Phys D Appl Phys. 2005; 38: 2543-55.
27. Xiao TG, Weis JA, Gayzik FS, Thomas A, Chiba A, Gurcan MN, et al. Applying dynamic contrast enhanced MSOT imaging to intratumoral pharmacokinetic modeling. Photoacoustics. 2018; 11: 28-35.
28. Chen Q, Liu X, Chen J, Zeng J, Cheng Z, Liu Z. A self-assembled albumin-based nanoprobe for *in vivo* ratiometric photoacoustic pH imaging. Adv Mater. 2015; 27: 6820-7.
29. Fan Q, Cheng K, Hu X, Ma X, Zhang R, Yang M, et al. Transferring biomarker into molecular probe: melanin nanoparticle as a naturally active platform for multimodality imaging. J Am Chem Soc. 2014; 136: 15185-94.
30. Fan Q, Cheng K, Yang Z, Zhang R, Yang M, Hu X, et al. Perylene-diimide-based nanoparticles as highly efficient photoacoustic agents for deep brain tumor imaging in living mice. Adv Mater. 2015; 27: 843-7.
31. Wang J, Chen F, Arconada-Alvarez SJ, Hartanto J, Yap L-P, Park R, et al. A nanoscale tool for photoacoustic-based measurements of clotting time and therapeutic drug monitoring of heparin. Nano Lett. 2016; 16: 6265-71.
32. Wang LV. Multiscale photoacoustic microscopy and computed tomography. Nat Photonics. 2009; 3: 503-9.
33. Antaris AL, Chen H, Cheng K, Sun Y, Hong G, Qu C, et al. A small-molecule dye for NIR-II imaging. Nat Mater. 2016; 15: 235-42.
34. Nagaoka R, Tabata T, Yoshizawa S, Umemura S-i, Saijo Y. Visualization of murine lymph vessels using photoacoustic imaging with contrast agents. Photoacoustics. 2018; 9: 39-48.
35. Homan K, Kim S, Chen Y-S, Wang B, Mallidi S, Emelianov S. Prospects of molecular photoacoustic imaging at 1064 nm wavelength. Opt Lett. 2010; 35: 2663-5.
36. Chen Y-S, Homan K, Xu D, Frey W, Emelianov S. Feasibility of contrast-enhanced photoacoustic liver imaging at a wavelength of 1064 nm. Biomedical Optics and 3-D Imaging. Miami, Florida: Optical Society of America; 2012. p. BM2B.7.
37. Ku G, Zhou M, Song S, Huang Q, Hazle J, Li C. Copper sulfide nanoparticles as a new class of photoacoustic contrast agent for deep tissue imaging at 1064 nm. ACS Nano. 2012; 6: 7489-96.
38. Hannah AS, VanderLaan D, Chen Y-S, Emelianov SY. Photoacoustic and ultrasound imaging using dual contrast perfluorocarbon nanodroplets triggered by laser pulses at 1064 nm. Biomed Opt Express. 2014; 5: 3042-52.
39. Zhou Y, Wang D, Zhang Y, Chitgupi U, Geng J, Wang Y, et al. A phosphorus phthalocyanine formulation with intense absorbance at 1000 nm for deep optical imaging. Theranostics. 2016; 6: 688-97.
40. Jiang Y, Upputuri PK, Xie C, Lyu Y, Zhang L, Xiong Q, et al. Broadband absorbing semiconducting polymer nanoparticles for photoacoustic imaging in second near-infrared window. Nano Lett. 2017; 17: 4964-9.
41. Wu J, You L, Lan L, Lee HJ, Chaudhry ST, Li R, et al. Semiconducting polymer nanoparticles for centimeters-deep photoacoustic imaging in the second near-infrared window. Adv Mater. 2017; 29: 1703403.
42. Park S, Park G, Kim J, Choi W, Jeong U, Kim C. Bi2 Se3 nanoplates for contrast-enhanced photoacoustic imaging at 1064 nm. Nanoscale. 2018; 10: 20548-58.
43. Sun T, Dou J-H, Liu S, Wang X, Zheng X, Wang Y, et al. Second near-infrared conjugated polymer nanoparticles for photoacoustic imaging and photothermal therapy. ACS Appl Mater Interfaces. 2018; 10: 7919-26.
44. Chen Y-S, Zhao Y, Yoon SJ, Gambhir SS, Emelianov S. Miniature gold nanorods for photoacoustic molecular imaging in the second near-infrared optical window. Nat Nanotechnol. 2019; 14: 465-72.
45. Huang K, Zhang Y, Lin J, Huang P. Nanomaterials for photoacoustic imaging in the second near-infrared window. Biomater Sci. 2019; 7: 472-9.
46. Upputuri PK, Pramanik M. Photoacoustic imaging in the second near-infrared window: a review. J Biomed Opt. 2019; 24: 040901.
47. Jiang Y, Upputuri PK, Xie C, Zeng Z, Sharma A, Zhen X, et al. Metabolizable semiconducting polymer nanoparticles for second near-infrared photoacoustic imaging. Adv Mater. 2019; 31: 1808166.
48. Miao Q, Pu K. Organic semiconducting agents for deep-tissue molecular imaging: second near-infrared fluorescence, self-luminescence, and photoacoustics. Adv Mater. 2018; 30: 1801778.
49. Wang Z, Zhen X, Upputuri PK, Jiang Y, Lau J, Pramanik M, et al. Redox-activatable and acid-enhanced nanotheranostics for second near-Infrared photoacoustic tomography and combined photothermal tumor therapy. ACS Nano. 2019; 13: 5816-25.
50. Wang Z, Upputuri PK, Zhen X, Zhang R, Jiang Y, Ai X, et al. pH-sensitive and biodegradable charge-transfer nanocomplex for second near-infrared photoacoustic tumor imaging. Nano Res. 2019; 12: 49-55.
51. Yin C, Wen G, Liu C, Yang B, Lin S, Huang J, et al. Organic semiconducting polymer nanoparticles for photoacoustic labeling and tracking of stem cells in the second near-infrared window. ACS Nano. 2018; 12: 12201-11.
52. Chitgupi U, Nyayapathi N, Kim J, Wang D, Sun B, Li C, et al. Surfactant-stripped micelles for NIR-II photoacoustic imaging through 12 cm of breast tissue and whole human breasts. Adv Mater. 2019; 31: 1902279.
53. Jung D, Park S, Lee C, Kim H. Recent progress on near-infrared photoacoustic imaging: imaging modality and organic semiconducting agents. Polymers. 2019; 11: 1693.
54. Kusamoto T, Nishihara H. Zero-, one-and two-dimensional bis (dithiolato) metal complexes with unique physical and chemical properties. Coord Chem Rev. 2019; 380: 419-39.
55. Schrauzer G, Mayweg V. Reaction of diphenylacetylene with nickel sulfides. J Am Chem Soc. 1962; 84: 3221.
56. Miao Q, Gao J, Wang Z, Yu H, Luo Y, Ma T. Syntheses and characterization of several nickel bis (dithiolene) complexes with strong and broad Near-IR absorption. Inorganica Chim Acta. 2011; 376: 619-27.
57. Dalgleish S, Matsushita MM, Hu L, Li B, Yoshikawa H, Awaga K. Utilizing photocurrent transients for dithiolene-based photodetection: stepwise improvements at communications relevant wavelengths. J Am Chem Soc. 2012; 134: 12742-50.
58. Mebrouk K, Debnath S, Fourmigué M, Camerel F. Photothermal control of the gelation properties of nickel bis (dithiolene) metallogelators under near-infrared irradiation. Langmuir. 2014; 30: 8592-7.
59. Mebrouk K, Camerel F, Jeannin O, Heinrich B, Donnio B, Fourmigué M. High photothermal activity within neutral nickel dithiolene complexes derived from imidazolium-based ionic liquids. Inorg Chem. 2016; 55: 1296-303.
60. Danhier F, Ansorena E, Silva JM, Coco R, Le Breton A, Préat V. PLGA-based nanoparticles: an overview of biomedical applications. J Control Release. 2012; 161: 505-22.
61. Li H, Ogusu K. Optical nonlinearities of Bis (4-dimethylaminodithiobenzil)-nickel solution in the nanosecond regime. Jpn J Appl Phys. 1998; 37: 5572.
62. Drexhage K, Muller-Westerhoff U. New Q-switch compounds for infrared lasers. IEEE J Quantum Electron. 1972; 8: 759.
63. Park S, Aglyamov SR, Emelianov S. 10A-5 beamforming for photoacoustic imaging using linear array transducer. IEEE Int Ultrason Symp. New York, New York: IEEE; 2007. p. 856-9.
64. Kim C, Jeon M, Wang LV. Nonionizing photoacoustic cystography *in vivo*. Opt Lett. 2011; 36: 3599-601.
65. Koo J, Jeon M, Oh Y, Kang HW, Kim J, Kim C, et al. *In vivo* non-ionizing photoacoustic mapping of sentinel lymph nodes and bladders with ICG-enhanced carbon nanotubes. Phys Med Biol. 2012; 57: 7853.
66. Jeon M, Jenkins S, Oh J, Kim J, Peterson T, Chen J, et al. Nonionizing photoacoustic cystography with near-infrared absorbing gold nanostructures as optical-opaque tracers. Nanomedicine. 2014; 9: 1377-88.
67. Kim C, Song KH, Gao F, Wang LV. Sentinel lymph nodes and lymphatic vessels: noninvasive dual-modality *in vivo* mapping by using indocyanine green in rats—volumetric spectroscopic photoacoustic imaging and planar fluorescence imaging. Radiology. 2010; 255: 442-50.
68. Lee C, Kwon W, Beack S, Lee D, Park Y, Kim H, et al. Biodegradable nitrogen-doped carbon nanodots for non-invasive photoacoustic imaging and photothermal therapy. Theranostics. 2016; 6: 2196-208.
69. Akers WJ, Kim C, Berezin M, Guo K, Fuhrhop R, Lanza GM, et al. Noninvasive photoacoustic and fluorescence sentinel lymph node identification using dye-loaded perfluorocarbon nanoparticles. ACS Nano. 2010; 5: 173-82.
70. Kim H, Chang JH. Multimodal photoacoustic imaging as a tool for sentinel lymph node identification and biopsy guidance. Biomed Eng Lett. 2018; 8: 183-91.
71. Kim J, Park S, Jung Y, Chang S, Park J, Zhang Y, et al. Programmable real-time clinical photoacoustic and ultrasound imaging system. Sci Rep. 2016; 6: 35137.
72. Choi W, Park E-Y, Jeon S, Kim C. Clinical photoacoustic imaging platforms. Biomed Eng Lett. 2018: 1-17.
73. Saha S, Jacklin R, Siddika A, Clayton G, Dua S, Smith S. Safety of radioactive sentinel node biopsy for breast cancer and the pregnant surgeon–a review. Int J Surg. 2016; 36: 298-304.
74. Bhutiani N, Samykutty A, McMasters KM, Egilmez NK, McNally LR. *In vivo* tracking of orally-administered particles within the gastrointestinal

tract of murine models using multispectral optoacoustic tomography. Photoacoustics. 2019; 13: 46-52.
75. Sivasubramanian K, Periyasamy V, Dienzo RA, Pramanik M. Hand-held, clinical dual mode ultrasound-photoacoustic imaging of rat urinary bladder and its applications. J Biophotonics. 2018; 11: e201700317.